CT14QED parton distribution functions from isolated photon production in deep inelastic scattering

Carl Schmidt,[*] Jon Pumplin,[†] Daniel Stump,[‡] and C.-P. Yuan[§]

Department of Physics and Astronomy, Michigan State University, East Lansing, Michigan 48824, USA

(Received 19 November 2015; published 16 June 2016)

We describe the implementation of quantum electrodynamic (QED) evolution at leading order (LO) along with quantum chromodynamic (QCD) evolution at next-to-leading order (NLO) in the CTEQ-TEA global analysis package. The inelastic contribution to the photon parton distribution function (PDF) is described by a two-parameter ansatz, coming from radiation off the valence quarks, and based on the CT14 NLO PDFs. Setting the two parameters to be equal allows us to completely specify the inelastic photon PDF in terms of the inelastic momentum fraction carried by the photon, p_0^γ, at the initial scale $Q_0 = 1.295$ GeV. We obtain constraints on the photon PDF by comparing with ZEUS data [S. Chekanov *et al.* (ZEUS Collaboration), Phys. Lett. B **687**, 16 (2010)] on the production of isolated photons in deep inelastic scattering, $ep \to e\gamma + X$. For this comparison we present a new perturbative calculation of the process that consistently combines the photon-initiated contribution with the quark-initiated contribution. Comparison with the data allows us to put a constraint at the 90% confidence level of $p_0^\gamma \lesssim 0.14\%$ for the inelastic photon PDF at the initial scale of $Q_0 = 1.295$ GeV in the one-parameter radiative ansatz. The resulting inelastic CT14QED PDFs will be made available to the public. In addition, we also provide CT14QEDinc PDFs, in which the *inclusive* photon PDF at the scale Q_0 is defined by the sum of the inelastic photon PDF and the elastic photon distribution obtained from the equivalent photon approximation.

DOI: 10.1103/PhysRevD.93.114015

I. INTRODUCTION

The high precision of current collider data requires comparable precision in the phenomenological predictions. The state of the art in high-energy calculations is at next-to-next-to-leading order (NNLO) in quantum chromodynamics (QCD). Consequently, major efforts have been undertaken to produce NNLO parton distribution functions (PDFs) from a global analysis of the available data. These include the CT14NNLO PDFs [1] as well as others [2–4], all of which include LHC data in the determination of the PDFs.

In this paper we describe the introduction of QED evolution at leading order (LO) with the next-to-leading order (NLO) QCD evolution in the same CTEQ global analysis package that was used to produce the CT14 PDFs [1]. Past studies of QED effects in global analysis have been done by the MRST [5] and the NNPDF [6] groups. We have checked our code against other QED + QCD evolution codes [7,8] and find good agreement.

The MRST and NNPDF analyses used different approaches for modeling the photon PDF. The MRST group used a parametrization for the photon PDF based on radiation off of "primordial" up and down quarks, with the photon radiation cut off at low scales by constituent or current quark masses [5]. The NNPDF group used a more general photon parametrization, which was then constrained by high-energy W, Z and Drell-Yan data at the LHC [6]. They found constraints on the size of the photon PDF, which was still consistent with zero at the initial scale of $\sqrt{2}$ GeV. As discussed by Martin and Ryskin [9], the photon PDF has a large *elastic* contribution in which the proton remains intact, in addition to the *inelastic* contribution in which the proton breaks into a multihadron final state.[1] Neither MRST nor NNPDF addresses these separate contributions to the photon PDF, although we can assume that the NNPDF photon is *inclusive*, containing both inelastic and elastic components, since it was constrained using inclusive Drell-Yan and vector boson data.

Given the limited amount of data to constrain the shape of the photon PDF, we will use a generalization of the MRST approach. We parametrize the inelastic contribution to the photon at the initial scale[2] $Q_0 = 1.295$ GeV by

[*]schmidt@pa.msu.edu
[†]pumplin@pa.msu.edu
[‡]stump@pa.msu.edu
[§]yuan@pa.msu.edu

[1]In Ref. [9], these two contributions are referred to as "coherent" and "incoherent," respectively.

[2]The initial scale $Q_0 = 1.295$ GeV is the same as that used in the standard CT14 PDF sets, and was chosen to be just below the input charm pole mass of $m_c = 1.3$ GeV.

$$f_{\gamma/p}(x,Q_0)=\frac{\alpha}{2\pi}(A_u e_u^2\tilde{P}_{\gamma q}\circ u^0(x)+A_d e_d^2\tilde{P}_{\gamma q}\circ d^0(x)), \tag{1}$$

where $\tilde{P}_{\gamma q}\circ f^0(x)$ is the convolution of the quark-to-photon splitting function $\tilde{P}_{\gamma q}(x)$ with the "primordial" quark distribution $f^0(x)$, which we take to be the initial CT14 NLO up and down valence distributions. We then set $A_u = A_d$ to obtain a single parameter family of photon distributions, which we can label by their initial inelastic momentum fraction p_γ^0. For comparison, in analogy with the MRST approach, we will also show results for a "current mass" (CM) photon distribution, given by defining $A_i = \ln(Q_0^2/Q_i^2)$, and setting the Q_i to the quark current masses; i.e., $Q_u = m_u = 6$ MeV and $Q_d = m_d = 10$ MeV.

We will constrain the inelastic photon PDF using data on deep inelastic scattering (DIS) with isolated photons from the ZEUS Collaboration [10]. The advantage of using this process is that the initial-state photon contributions are at leading order in the perturbation expansion. In contrast, the initial-state photon contribution to Drell-Yan or W and Z production is suppressed by factors of (α/α_s) relative to the leading quark-antiquark production. However, to use the DIS-plus-photon data, we will first need to address some technical issues relating to the combination of different subprocess contributions to the observed final state.

The organization of this paper is as follows: In Sec. II we describe the inclusion of QED evolution in the CTEQ global analysis code and give more details about our initial PDF parametrizations. In Sec. III we discuss constraints on the photon PDF coming from the CT14 global analysis data set and from the ZEUS DIS with isolated photon data. In this section we present a new calculation for the DIS-plus-isolated-photon process, which consistently combines the photon-initiated contribution with the quark-initiated contribution. We show that these data give significant constraints on the initial photon PDF. In Sec. IV we discuss our findings and give conclusions. We also include an Appendix, where we show comparisons between our QCD + QED evolution code and other publicly available codes.

II. INCORPORATION OF QED EFFECTS IN CTEQ-TEA GLOBAL ANALYSIS

In this section we discuss the implementation of the QED evolution and the initial photon PDF in the context of the CTEQ-TEA global analysis program.

A. QCD-plus-QED evolution

The evolution of the PDFs, $f(x,\mu_F)$, including QED contributions at leading order (LO) and QCD contributions at higher orders, is described by the equations

$$\begin{aligned}
\frac{df_{q_i}}{dt}&=\frac{\alpha_s}{2\pi}\left(\sum_j(P_{q_iq_j}\circ f_{q_j}+P_{q_i\bar{q}_j}\circ f_{\bar{q}_j})+P_{qg}\circ f_g\right)\\
&\quad+\frac{\alpha}{2\pi}e_i^2(\tilde{P}_{qq}^{(0)}\circ f_{q_i}+\tilde{P}_{q\gamma}^{(0)}\circ f_\gamma),\\
\frac{df_{\bar{q}_i}}{dt}&=\frac{\alpha_s}{2\pi}\left(\sum_j(P_{\bar{q}_i\bar{q}_j}\circ f_{\bar{q}_j}+P_{\bar{q}_iq_j}\circ f_{q_j})+P_{qg}\circ f_g\right)\\
&\quad+\frac{\alpha}{2\pi}e_i^2(\tilde{P}_{qq}^{(0)}\circ f_{\bar{q}_i}+\tilde{P}_{q\gamma}^{(0)}\circ f_\gamma),\\
\frac{df_g}{dt}&=\frac{\alpha_s}{2\pi}\left(P_{gg}\circ f_g+\sum_i P_{gq}\circ(f_{q_i}+f_{\bar{q}_i})\right),\\
\frac{df_\gamma}{dt}&=\frac{\alpha}{2\pi}\left(\tilde{P}_{\gamma\gamma}^{(0)}\circ f_\gamma+\sum_i e_i^2\tilde{P}_{\gamma q}^{(0)}\circ(f_{q_i}+f_{\bar{q}_i})\right),
\end{aligned} \tag{2}$$

where $t=\ln\mu_F^2$, the indices i and j run over active quark flavors, and the convolution is defined by

$$(P_{ab}\circ f_b)(x,\mu_F)=\int_0^1 dz\int_0^1 dy\,\delta(zy-x)P_{ab}(z)f_b(y,\mu_F). \tag{3}$$

The QCD splitting functions, given by

$$P_{ab}=\sum_n\left(\frac{\alpha_s}{2\pi}\right)^n P_{ab}^{(n)}, \tag{4}$$

are known up to $n=2$, next-to-next-to-leading order (NNLO) [11,12]. The LO QED splitting functions can be extracted from the LO QCD splitting functions, giving

$$\begin{aligned}
\tilde{P}_{qq}^{(0)}(z)&=\frac{1+z^2}{(1-z)_+}+\frac{3}{2}\delta(1-z),\\
\tilde{P}_{q\gamma}^{(0)}(z)&=N_c[z^2+(1-z)^2],\\
\tilde{P}_{\gamma q}^{(0)}(z)&=\frac{1+(1-z)^2}{z},
\end{aligned} \tag{5}$$

$$\tilde{P}_{\gamma\gamma}^{(0)}(z)=-\frac{2}{3}N_c\sum_i e_i^2\delta(1-z), \tag{6}$$

where $N_c=3$ is the number of colors.

We have modified the Fortran NLO evolution code evolve, which was used for previous CTEQ-TEA PDFs (CTEQ6-6.6 [13–16] and CT09 [17]), to include the LO QED contributions. This code solves the evolution equations directly in x space, so that the only new technical issue introduced by the QED corrections is the separation of the quark singlet distributions into separate up and down contributions, based on the quark charges. We have checked our evolution code against the public QCD + QED codes, partonevolution [7,18] and APFEL [8], and we

find good agreement. Details of this comparison are given in the Appendix.

B. Initial photon PDFs

The initial photon PDF at the scale Q_0 is a nonperturbative input that must be obtained by a fit to data. Even a choice of zero initial photon PDF is ambiguous, since it depends on the arbitrary scale Q_0. So far, there have been two different approaches to the initial photon PDF. In the MRST analysis [5], the initial photon PDF was given by an ansatz, obtained from radiation off primordial-valence up- and down-quark distributions, cut off at low scales given by the current quark masses, $m_u = 6$ MeV and $m_d = 10$ MeV, or by constituent quark masses $m_U = m_D = 300$ MeV. Alternatively, the NNPDF approach [6] was to use a general parametrization for the initial photon PDF to be constrained by high-energy W, Z, and Drell-Yan production at the LHC.

In this work we will use a generalization of the MRST ansatz, but we must first address a subtlety of the photon PDF. Unlike the case for colored partons, the photon PDF has a large elastic component, in which the proton remains intact [9]. This is in addition to the inelastic component, in which the proton dissociates. The elastic component can be parametrized by the equivalent photon approximation (EPA) [19], which involves an integration over the proton electromagnetic form factors. For this work, we focus on the inelastic component, which we parametrize by a radiative ansatz, but with free parameters to be fit by data. Given the weak constraints from data on the photon PDF, we find it useful to limit the number of parameters to one or two for the time being. We shall see that the ZEUS DIS-plus-isolated-photon data [10] constrains the inelastic photon PDF roughly in the range $10^{-3} < x < 2 \times 10^{-2}$ for $16 < Q^2 < 300$ GeV^2.

We parametrize the inelastic contribution to the initial photon PDFs in the proton and neutron by

$$f_{\gamma/p}(x,Q_0) = \frac{\alpha}{2\pi}\left(A_u e_u^2 \tilde{P}_{\gamma q} \circ u^0(x) + A_d e_d^2 \tilde{P}_{\gamma q} \circ d^0(x)\right),$$
$$f_{\gamma/n}(x,Q_0) = \frac{\alpha}{2\pi}\left(A_u e_u^2 \tilde{P}_{\gamma q} \circ d^0(x) + A_d e_d^2 \tilde{P}_{\gamma q} \circ u^0(x)\right), \tag{7}$$

where u^0 and d^0 are "primordial" valence-type distributions in the proton, and the initial photon PDF in the neutron is obtained by an approximate isospin symmetry. Defining $A_i = \ln(Q_0^2/Q_i^2)$, we can trade the parameters A_i for mass scales Q_i, and we see that the nonperturbative inputs $f_{\gamma/(p,n)}(x,Q_0)$ are modeled by the radiation of a single photon off the "primordial" quarks, with a collinear cutoff given by the scales Q_i. The MRST initial photon PDFs can be obtained from this parametrization by setting $Q_0 = 1$ GeV, using the functions for u_0 and d_0 given in Ref. [5], and letting Q_u and Q_d be either the constituent or current quark masses. For our analysis, we use $Q_0 = 1.295$ GeV as in CT14, and we set

$$u_0(x) = u_V^p(x,Q_0) = f_{u/p}(x,Q_0^2) - f_{\bar{u}/p}(x,Q_0^2),$$
$$d_0(x) = d_V^p(x,Q_0) = f_{d/p}(x,Q_0^2) - f_{\bar{d}/p}(x,Q_0^2), \tag{8}$$

the initial up and down CT14 NLO valence distributions in the proton.

The presence of the photon PDF violates isospin between the neutron and proton. Continuing with the radiative ansatz and working to first order in α, we can neglect the isospin violation in the gluon and sea-quark PDFs [5] and use

$$f_{g/p}(x,Q_0) = f_{g/n}(x,Q_0),$$
$$f_{\bar{q}/p}(x,Q_0) = f_{\bar{q}/n}(x,Q_0) \quad \text{for } \bar{q} = \bar{u},\bar{d},\bar{s},\bar{c},\bar{b},$$
$$f_{q/p}(x,Q_0) = f_{q/n}(x,Q_0) \quad \text{for } q = s,c,b. \tag{9}$$

For the valence quarks at first order in α, the radiative ansatz plus approximate isospin symmetry implies

$$u_V^p(x,Q_0) \approx u^0(x) + \frac{\alpha}{2\pi} A_u e_u^2 \tilde{P}_{qq} \circ u^0(x),$$
$$d_V^p(x,Q_0) \approx d^0(x) + \frac{\alpha}{2\pi} A_d e_d^2 \tilde{P}_{qq} \circ d^0(x),$$
$$u_V^n(x,Q_0) \approx d^0(x) + \frac{\alpha}{2\pi} A_u e_u^2 \tilde{P}_{qq} \circ d^0(x),$$
$$d_V^n(x,Q_0) \approx u^0(x) + \frac{\alpha}{2\pi} A_d e_d^2 \tilde{P}_{qq} \circ u^0(x). \tag{10}$$

This suggests a consistent set of PDFs for the valence quarks in the neutron given by

$$u_V^n(x,Q_0) = d_V^p(x,Q_0) + \frac{\alpha}{2\pi}(A_u e_u^2 - A_d e_d^2)\tilde{P}_{qq} \circ d^0(x),$$
$$d_V^n(x,Q_0) = u_V^p(x,Q_0) + \frac{\alpha}{2\pi}(A_d e_d^2 - A_u e_u^2)\tilde{P}_{qq} \circ u^0(x). \tag{11}$$

Note that Eqs. (7) and (11) together ensure that if the number and momentum sum rules (including the photon contribution) are satisfied for the PDFs in the proton, they are automatically satisfied for the PDFs in the neutron,[3] regardless of the choices for u^0 and d^0. Again, for our analysis, we choose u_0 and d_0 to equal the initial up and down CT14 NLO valence distributions in the proton. Thus, from Eqs. (7)–(9) and (11) we can obtain the quark, gluon, and photon PDFs in both the proton and neutron in terms of the parametrization of the quark and gluon PDFs in the proton, plus the two additional parameters A_u and A_d.

[3]This simple approximate isospin symmetry is broken by the inclusion of the elastic component of the photon PDF, since there is no corresponding elastic photon in the neutron.

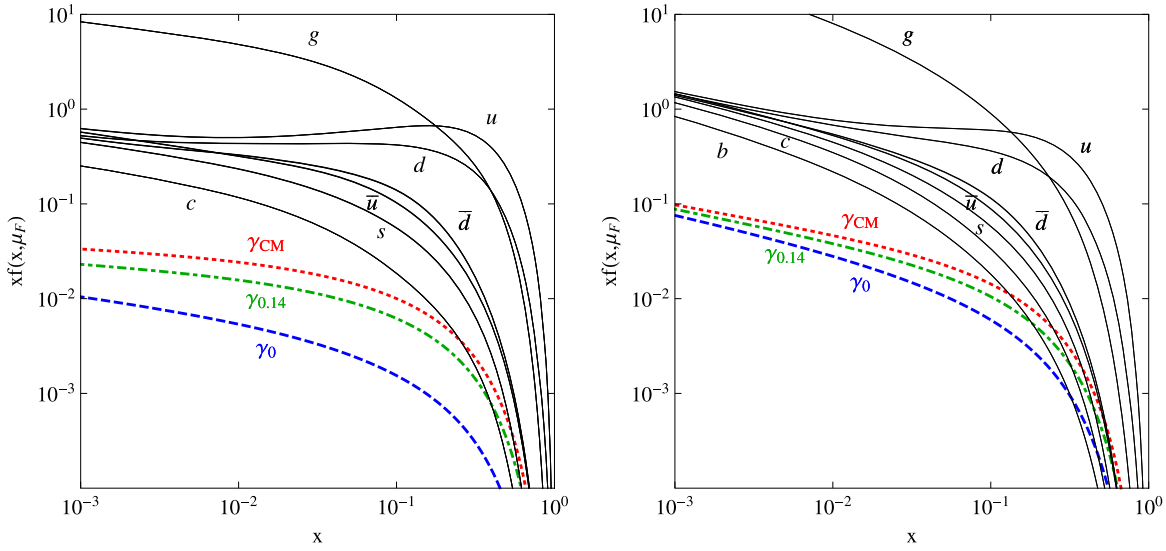

FIG. 1. Plots of $xf(x,\mu_F)$ for $\mu_F = 3.2$ GeV (left) and $\mu_F = 85$ GeV (right). Three representative photon PDFs are plotted: the "current mass" photon PDF ($\gamma_{\rm CM}$, red dotted), and photon PDFs with initial inelastic photon momenta fractions of $p_0^\gamma = 0$ and 0.14% (γ_0, blue dashed, and $\gamma_{0.14}$, green dot-dashed, respectively). The effects of the different initial photon PDFs on the quark and gluon PDFs are imperceptible in these plots.

For this paper, we shall make the further simplification of $A_u = A_d$, which corresponds to cutting off the radiation from both valence quarks at the same scale. With this choice, everything is specified by one additional parameter, which can be taken to be the cutoff scale $Q_{\rm cut} = Q_u = Q_d$, defined by $A_u = A_d = \ln(Q_0^2/Q_{\rm cut}^2)$. Alternatively, we can trade this parameter for the initial inelastic photon momentum fraction in the proton:

$$p_0^\gamma = \int_0^1 dx x f_{\gamma/p}(x, Q_0). \tag{12}$$

For the remainder of this paper, unless otherwise specified, the photon PDFs will be in this one-parameter radiation ansatz labeled by p_0^γ. For comparison purposes, we will make one exception to this by defining a "current mass" (CM) photon PDF, analogous to the MRST current mass PDF, and given by $A_i = \ln(Q_0^2/Q_i^2)$ with $Q_u = m_u = 6$ MeV and $Q_d = m_d = 10$ MeV. For this choice the initial inelastic photon momentum fraction is determined to be $p_0^\gamma = 0.26\%$. For all other partons in our analysis we use the CT14 NLO initial distributions, except that to maintain a total momentum fraction of 1, we renormalize the initial up, down, and strange sea-quark distributions, to account for the additional photon momentum fraction. Given that the relevant photon momentum fractions are very small, we find that this reduces the sea-quark distributions by typically less than 1%, and it is inconsequential in our analysis. (The sea-quark distributions are reduced by 0.9% for $p_0^\gamma = 0.14\%$, and they are reduced by 1.6% for the CM photon PDF.) In Fig. 1 we plot the quantity $xf(x,\mu_F)$ for three representative photon PDFs, relative to the quark and gluon PDFs, at the scales $\mu_F = 3.2$ GeV and $\mu_F = 85$ GeV. We note that the effect of the initial photon PDF and the QED evolution on the quark and gluon PDFs is imperceptible in these plots. For the photon PDF, we plot for $p_0^\gamma = 0\%$ ($Q_{\rm cut} = Q_0 = 1.295$ GeV) and for $p_0^\gamma = 0.14\%$ ($Q_{\rm cut} = 71$ MeV), and for the CM photon PDF.

III. CONSTRAINTS ON THE PHOTON PDF

A. Constraints from the CT14 data set

The constraints on the photon PDF from the DIS and Tevatron data, used in the CT14 analysis, are relatively weak. These come from two main sources: isospin violation effects in nuclear scattering and constraints from the momentum sum rule. In general, isospin violation will arise through QED evolution, as well as from the initial conditions given by Eq. (11). This isospin violation can be seen in Fig. 2, where we plot $f_{d/n}(x,\mu_F)/f_{u/p}(x,\mu_F)$ and $f_{u/n}(x,\mu_F)/f_{d/p}(x,\mu_F)$ for several values of μ_F for the case where the initial photon PDF is zero, and for the case where the initial photon is the CM choice. Note that the isospin violation is small and most important at large x. Given that cuts of $W^2 = Q^2(1/x - 1) > 12$ GeV^2, applied to enforce perturbativity in the calculations, typically require $x \lesssim 0.2$–0.4, we expect constraints from isospin violation to be small in the present data, as observed in the MRST analysis [5].

Constraints from the momentum sum rule arise because any momentum carried by the photon implies less momentum available for the quark and gluon PDFs. In this way, constraints from data on the colored parton PDFs indirectly impact the photon PDF. We have performed a preliminary analysis using the data sets included for CT10 [20]. For a fixed initial photon momentum fraction, with the photon

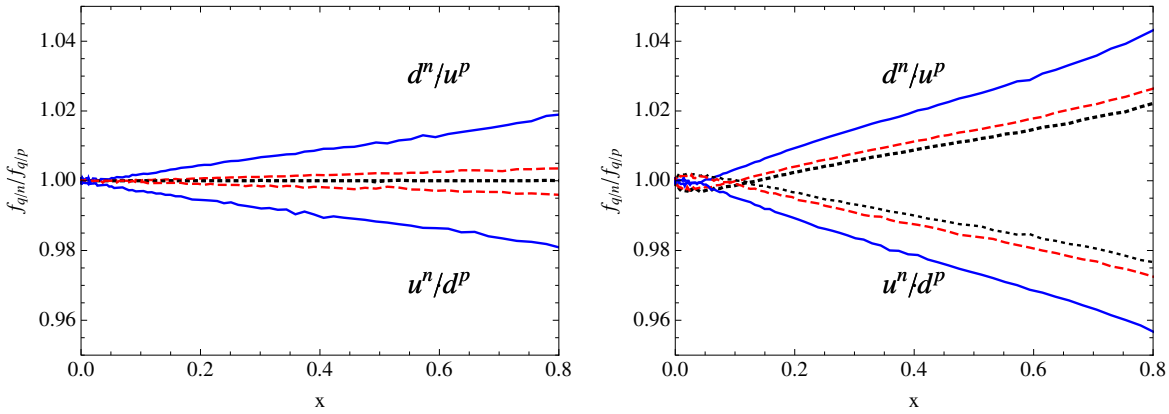

FIG. 2. Plots of $f_{d/n}(x,\mu_F)/f_{u/p}(x,\mu_F)$ and $f_{u/n}(x,\mu_F)/f_{d/p}(x,\mu_F)$ for $\mu_F = 1.3$ GeV (black dots), 3.2 GeV (red dashes), and 85 GeV (blue solid). The left plot is for zero initial photon momentum, and the right plot is for the CM photon PDF.

PDF parametrized as discussed in Sec. II, we minimized the global χ^2 by varying the quark and gluon PDFs. Using the usual CTEQ-TEA choice of $\Delta\chi^2 < 100$ tolerance, we obtain a limit on the photon momentum fraction of $p_0^\gamma < 5.6\%$ at the 90% confidence level, which is similar in magnitude to the results found by the MRST and NNPDF analyses. The best fit for the initial photon momentum fraction from this global analysis is $p_0^\gamma = 1.2\%$, but with only a small change of $\Delta\chi^2 = -7$, relative to the fit with $p_0^\gamma = 0\%$. For comparison, we find the elastic contribution to the initial photon momentum fraction, as calculated in the equivalent photon approximation, to be $p_{0,\text{elastic}}^\gamma = 0.15\%$.

Unfortunately, this limit on the initial photon momentum fraction is much larger than one would expect for a photon PDF. In the analysis of the NNPDF group, additional constraints were made on the initial photon PDF by including LHC data on high-energy W, Z, and Drell-Yan production, and comparing with theoretical predictions that included photon initial-state contributions. Although the photon-induced contribution to these processes is small compared to the dominant quark-antiquark annihilation subprocess, the precision of these measurements was enough to substantially increase the constraints on the photon PDF [6]. However, the small relative contribution of the photon-photon subprocess puts a stringent requirement on the precision needed for both experimental and theoretical analyses. Any small misjudgment of systematic errors on the experimental side or uncalculated higher-order corrections on the theoretical side could have a significant effect on the extraction of the photon PDF. In particular, given that the initial photon PDF is nominally of order α, one might expect that the uncalculated $\mathcal{O}(\alpha^2)$ quark-initiated contributions to Drell-Yan production would contribute at the same level as the photon-initiated contributions. For this reason, we consider a different experimental process, isolated photon production in DIS, to constrain the photon PDF.

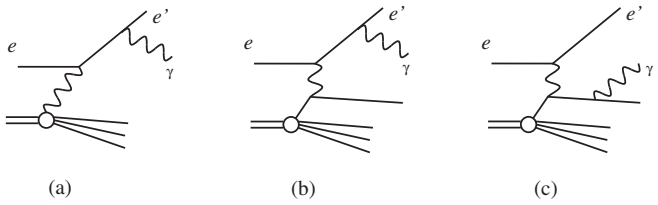

FIG. 3. Amplitudes for the process $ep \to e\gamma + X$. For each diagram shown, there is an additional diagram where the photon is emitted off the initial-state lepton or quark.

B. Calculation of the process $ep \to e\gamma + X$

At the partonic level, the process of DIS with isolated photon occurs at LO through Compton scattering of a photon coming from the proton off the lepton, as shown in Fig. 3(a). Thus, this process probes the photon PDF at LO, having no large backgrounds with which to compete. However, the quark-initiated subprocess shown in Figs. 3(b) and 3(c), while formally suppressed by $\mathcal{O}(\alpha)$, is just as large because of the small size of f_γ relative to f_q. In fact, if we consider the photon PDF to be $\mathcal{O}(\alpha)$, then the photon-initiated subprocess and the quark-initiated subprocess are actually the same order in α. Thus, the correct way to calculate the cross section for DIS with isolated photons is to include both subprocesses consistently without double-counting.

In the literature, there have been two approaches to calculations of the process $ep \to e\gamma + X$. The calculation of MRST [5], which was preceded by studies of Blümlein *et al.* [21–23], included just the photon-initiated contribution of Fig. 3(a). The calculation of Gehrmann–De Ridder, Gehrmann, and Poulsen (GGP) [24,25] included just the quark-initiated contributions of Figs. 3(b) and 3(c). In the GGP analysis, it was found convenient to make the Lorentz-invariant separation of the cross section into three components, depending on the fermion line off which the final-state photon is emitted: LL for emission off the

lepton line, given by the square of the partonic amplitude in Fig. 3(b); QQ for emission off the quark line, given by the square of the partonic amplitude in Fig. 3(c); and QL for the interference between the two sets of diagrams.[4] In the GGP calculation, a cut on the outgoing quark was necessary to remove the divergence in the amplitude as the photon off-shell-ness went to zero in the LL amplitude. A hybrid calculation was also considered by the ZEUS Collaboration in their analysis of the DIS-plus-isolated-photon data [10], where the LL component of the quark-initiated subprocess of GGP was replaced by the photon-initiated subprocess of MRST.

In this section we introduce a consistent and systematic method of combining the photon- and quark-initiated subprocesses, which also reduces the factorization scale dependence of either calculation. First, consider the calculation of the differential cross section as a power series in α without consideration of the relative sizes of f_γ and f_q. It can be written as a convolution over partonic cross sections

$$d\sigma = \sum_a \int_0^1 d\xi f_a(\xi, \mu_F) d\hat{\sigma}_a, \tag{13}$$

where each of the partonic cross sections can be expanded in a power series in α:

$$d\hat{\sigma}_a = \sum_n d\hat{\sigma}_a^{(n)}. \tag{14}$$

The diagram in Fig. 3(a) corresponds to a LO contribution ($a = \gamma; n = 0$), while the diagrams in Figs. 3(b) and 3(c) correspond to NLO contributions ($a = q, \bar{q}; n = 1$). Through NLO in α, the cross section can still be written as a sum of LL, QQ, and QL components,

$$d\sigma = d\sigma^{(LL)} + d\sigma^{(QQ)} + d\sigma^{(QL)}, \tag{15}$$

where the LL component also includes the photon-initiated contribution,

$$d\sigma^{(LL)} = \int_0^1 d\xi \left[f_\gamma(\xi, \mu_F) d\hat{\sigma}_\gamma + \sum_{a=q,\bar{q}} f_a(\xi, \mu_F) d\hat{\sigma}_a^{(LL)} \right]. \tag{16}$$

Using the modified minimal subtraction ($\overline{\text{MS}}$) scheme, we can factorize the initial-state singularity from the NLO quark-initiated subprocess into the definition of the photon PDF, leaving a NLO subprocess cross section,

$$d\hat{\sigma}_q^{(1,LL)} = d\sigma_q^{(1,LL)} + \frac{\alpha}{2\pi} \left(\frac{4\pi\mu_R^2}{\mu_F^2} \right)^\epsilon \frac{1}{\epsilon\Gamma(1-\epsilon)} \times \int_0^1 dz \tilde{P}_{\gamma q}(z) d\hat{\sigma}_\gamma^{(0)}(z\xi), \tag{17}$$

where the first term on the right-hand side, $d\sigma_q^{(1,LL)}$, is the hard partonic quark-induced subprocess, and the second term is the collinear subtraction counterterm. Here, we have distinguished the renormalization scale μ_R from the factorization scale μ_F, and we explicitly note that the initial-state collinear singularity cancels within the LL component. Calculating everything in dimensional regularization with $4 - 2\epsilon$ dimensions, the combined LL component of the NLO quark-initiated subprocess cross section, $d\hat{\sigma}_q^{(1,LL)}$, is finite as $\epsilon \to 0$.

In principle, there are additional virtual and real contributions at NLO in α besides the quark-initiated contributions. However, all other NLO terms are proportional to f_γ, which is in fact suppressed by an amount of order α relative to f_q, as seen in the previous section. Thus, by keeping the photon-initiated contribution at LO and the quark-initiated contributions at NLO, and including the collinear-subtraction counterterm of Eq. (17), we have a well-defined calculation in the $\overline{\text{MS}}$ scheme, while maintaining all contributions of the same size in α. Note that this is reminiscent of the ACOT scheme [26] for including charm and bottom quark PDFs, although for the photon, there is no equivalent of the fixed-flavor scheme, due to its zero mass and the consequently nonperturbative photon PDF.

The calculations of the QQ and QL components are identical to those in the GGP calculation. For the kinematics of interest to us, the QL component is negligible, but it is included for completeness. The QQ contribution has a final-state singularity, when the photon and final-state quark become collinear, which can be handled by including a fragmentation contribution and an associated collinear subtraction counterterm in the $\overline{\text{MS}}$ scheme. Thus, we obtain

$$d\hat{\sigma}_q^{(1,QQ)} = d\sigma_q^{(1,QQ)} + \frac{\alpha}{2\pi} \left(\frac{4\pi\mu_R^2}{\mu_f^2} \right)^\epsilon \frac{1}{\epsilon\Gamma(1-\epsilon)} \times \int_0^1 dz \tilde{P}_{\gamma q}(z) d\hat{\sigma}_{eq\to e'Q'}|_{Q'=k'/z} + \int_0^1 dz D_{\gamma/Q'}(z, \mu_f) d\hat{\sigma}_{eq\to e'Q'}|_{Q'=k'/z}, \tag{18}$$

where $d\sigma_q^{(1,QQ)}$ is the hard partonic subprocess, $d\hat{\sigma}_{eq\to e'Q'}$ is the LO subprocess cross section for $eq \to e'Q'$, and $D_{\gamma/Q'}(z, \mu_F)$ is the fragmentation function for finding the photon (with momentum k') in the quark Q' (with momentum Q'), with momentum fraction z at the fragmentation scale μ_f. The singularities in the first two terms on the right-hand side of this equation cancel as $\epsilon \to 0$. We

[4]Note that each of the diagrams in Fig. 3 actually represents two Feynman diagrams, where the final-state photon is emitted off the initial-state lepton or quark as well as off the final-state lepton or quark.

will discuss the choice for the fragmentation function in the next subsection.

We have calculated the LL and the QQ components of the cross section, using the subtraction method to handle the collinear divergences [27] in the hard cross-section term. Following this method, we subtract a term with a two-particle final state mapped onto a three-particle final state, with the third particle phase space unintegrated, and then add back the exact same term with the third particle phase space integrated out. The subtraction term is designed to have the same collinear-singular limit as the hard term in the same region of phase space of the third particle, so that the hard cross section term minus the subtraction is integrable in $d = 4$ dimensions, while the $1/\epsilon$ singularities in the remaining terms cancel. Using this method, we obtain for the LL quark-initiated contribution

$$d\hat{\sigma}_q^{(1,LL)} = \left(d\sigma_q^{(1,LL)} - d\sigma_{q(\mathrm{sub})}^{(1,LL)}\right) + d\hat{\sigma}_{q(\mathrm{AP})}^{(1,LL)}, \tag{19}$$

where

$$d\hat{\sigma}_{q(\mathrm{AP})}^{(1,LL)} = \int_0^1 dz \frac{\alpha}{2\pi}\left[\tilde{P}_{\gamma q}(z)\ln\left(\frac{s\xi(1-z)^2}{\mu_F^2}\right) + e_q^2 z\right] \times d\hat{\sigma}_\gamma^{(0)}(z\xi). \tag{20}$$

The hard term minus the subtraction term can be written as an integral over the phase space of the additional quark:

$$(d\sigma_q^{(1,LL)} - d\sigma_{q(\mathrm{sub})}^{(1,LL)}) = \int_0^1 dw \int_0^{2\pi} \frac{d\phi}{2\pi}\left(2\pi \frac{d^2(d\sigma_q^{(1,QQ)})}{dw d\phi} - \int_0^1 dz \frac{\alpha}{2\pi w}\tilde{P}_{\gamma q}(z) d\hat{\sigma}_\gamma^{(0)}(z\xi)\right), \tag{21}$$

where $w = (1-\cos\theta)/2$, with θ and ϕ the scattering angles of the final-state quark in the initial parton-parton center-of-momentum frame. Note that the hard term on the right-hand side is treated with three-body final-state phase space, while the subtraction term is treated with two-body final-state phase space.

Similarly, we obtain for the QQ contribution

$$d\hat{\sigma}_q^{(1,QQ)} = \left(d\sigma_q^{(1,QQ)} - d\sigma_{q(\mathrm{sub})}^{(1,QQ)}\right) + d\hat{\sigma}_{q(\mathrm{frag})}^{(1,QQ)}, \tag{22}$$

where

$$d\hat{\sigma}_{q(\mathrm{frag})}^{(1,QQ)} = \int_0^1 dz \left\{ D_{\gamma/Q'}(z,\mu_f) + \frac{\alpha}{2\pi}\left[\tilde{P}_{\gamma q}(z)\ln\left(\frac{s\xi z^2(1-z)}{\mu_f^2}\right) + e_q^2 z\right]\right\} d\hat{\sigma}_{eq\to e'Q'}. \tag{23}$$

The hard term minus the subtraction term can be written

$$(d\sigma_q^{(1,QQ)} - d\sigma_{q(\mathrm{sub})}^{(1,QQ)}) = \int_0^1 d\tilde{w} \int_0^{2\pi} \frac{d\tilde{\phi}}{2\pi}\left(2\pi \frac{d^2(d\sigma_q^{(1,LL)})}{d\tilde{w} d\tilde{\phi}} - \int_0^1 dz \frac{\alpha}{2\pi\tilde{w}}\tilde{P}_{\gamma q}(z) d\hat{\sigma}_{eq\to e'Q'}\right), \tag{24}$$

where in this case we have found it convenient to use a different parametrization of the final-state quark phase space. Letting $qe \to q'e'\gamma$ be the hard partonic subprocess, we use $\tilde{w} = (1-\cos\tilde{\theta})/2$, where $\tilde{\theta}$ is the angle between q' and γ in the $q'e'$ center-of-momentum frame and $\tilde{\phi}$ is the azimuthal angle between the $qe\gamma$ plane and the $q'e'\gamma$ plane. As before, the hard term on the right-hand side is treated with three-body final-state phase space, while in this case the subtraction term and the fragmentation term are treated in the limit where the final-state photon and quark are collinear, with momenta satisfying $k' = zQ'$ and $q' = (1-z)Q'$.

C. ZEUS experimental cuts and photon isolation

The ZEUS experiment [10] used proton and lepton beam energies of $E_p = 920$ GeV and $E_\ell = 27.5$ GeV, respectively, corresponding to a center-of-mass energy and rapidity of

$$\sqrt{s} = 2\sqrt{E_p E_\ell} = 318 \text{ GeV}, \qquad Y = \frac{1}{2}\ln\frac{E_p}{E_\ell} = 1.76, \tag{25}$$

respectively. (We neglect the proton mass, m_p, in all calculations here.) For the process $ep \to e\gamma + X$, with momentum satisfying $\ell + p = \ell' + k' + p'_X$, one can define the standard DIS variables that describe the kinematics of the scattered lepton, $Q^2 = -(\ell - \ell')^2$, $y = p\cdot(\ell - \ell')/(p\cdot\ell)$, and $x = Q^2/(sy)$. The ZEUS Collaboration measured distributions for two leptonic variables Q and x, and for two photonic variables, $E_{\perp\gamma}$ and η_γ, the transverse energy and pseudorapidity of the photon, respectively. The collaboration combined data that were 59.1% $e^- p$ and 40.9% $e^+ p$ scattering. Note that the sign of the charged lepton has no effect on the LL or QQ components of the calculation, but the combination of the two charged lepton contributions produces a significant cancellation of the already small QL component, so that it is negligible in the analysis.

The kinematic region defined by the experiment was

$$\begin{aligned} 10 \text{ GeV}^2 < Q^2 < 350 \text{ GeV}^2, \\ E'_\ell > 10 \text{ GeV}, \\ 139.8^\circ < \theta'_\ell < 171.8^\circ, \\ 4 \text{ GeV} < E_{\perp\gamma} < 15 \text{ GeV}, \\ -0.7 < \eta_\gamma < 0.9. \end{aligned} \tag{26}$$

The cut on the final-state lepton angle, θ'_ℓ, can be written in terms of its rapidity as

$$-2.6355 < \eta'_\ell < -1.0053. \tag{27}$$

There are two additional cuts that require discussion. The experimentalists reported a cut of $W_X > 5$ GeV, where $W_X^2 = (p + \ell - \ell' - k')^2$. Naively, this cut looks problematic because it would remove the photon-initiated contribution, which occurs at exactly $W_X = 0$. However, upon closer investigation it appears that this cut was only applied to the theoretical and Monte Carlo calculations. To quote from Ref. [28], "The keen reader will note that no such cut was applied at the detector level. This proved impossible due to the poor W_X resolution at detector level and poor description of the data by MC…." The relevant detector-level cut was the requirement of at least one reconstructed track, well separated from the lepton, which was used to ensure some hadronic activity and to remove deeply virtual Compton scattering events. After this cut, it was found that the number of events in the Monte Carlo calculations with $W_X < 5$ GeV was negligible. For our purposes, we interpret the forward track cut as a requirement to tag inelastic events, and we include no explicit W_X cut.

Note that the forward track cut should equally remove elastic isolated photon events, and so remove the contribution from the elastic part of the photon PDF. In this way, the ZEUS data probe only the inelastic part of the photon PDF, and therefore, we only include this inelastic contribution in comparison with the experimental data. In doing so, we have made the approximation $f_{\gamma,\text{inclusive}}(x,Q) \approx f_{\gamma,\text{elastic}}(x,Q) + f_{\gamma,\text{inelastic}}(x,Q)$; i.e., the elastic and inelastic components of the photon PDF evolve separately. This approximation is good because $f_{\gamma,\text{elastic}}(x,Q)$ changes very little from Q_0 to Q due to the rapid falloff of the proton electromagnetic form factor, while the inelastic contribution evolves additively,

$$f_{\gamma,\text{inelastic}}(x,Q) \approx f_{\gamma,\text{inelastic}}(x,Q_0) + \sum_i \int_{Q_0^2}^{Q^2} \frac{dQ^2}{Q^2}\frac{\alpha}{2\pi} \times e_i^2 \tilde{P}_{\gamma q}^{(0)} \circ (f_{q_i} + f_{\bar{q}_i})(x,Q), \tag{28}$$

up to corrections suppressed by extra factors of α. We have verified by explicit calculation that this additive approximation replicates the consistently evolved inclusive photon PDF, with errors that are far smaller than other theoretical uncertainties that we will discuss below.

The second additional important cut is the isolation cut on the photon, enforcing that 90% of the energy in the jet containing the photon belongs to the photon, where jets are formed with the k_T cluster algorithm with parameter $R = 1.0$. We will model this isolation cut in our calculation in two different ways. First, we can model the experimental cut at the parton level, requiring $E_\gamma/(E_q + E_\gamma) > 0.9$ if the photon-quark separation satisfies $r = \Delta R_{\gamma q} = ((\Delta\eta_{\gamma q})^2 + (\Delta\phi_{\gamma q})^2)^{1/2} < 1$. For later reference, we call this the "sharp" isolation cut. Since this does not completely remove the quark-photon collinear singularity, the theoretical calculation of the QQ component will depend on the choice of the quark-to-photon fragmentation function $D_{\gamma/Q'}(z,\mu_f)$. For this, we use the LO fragmentation function determined by the ALEPH Collaboration [29], parametrized by

$$D_{\gamma/Q'}(z,\mu_f) = \frac{\alpha}{2\pi}\left[\tilde{P}_{\gamma q}(z)\ln\left(\frac{\mu_f^2}{\mu_0^2(1-z)^2}\right) + e_q^2 C_0\right],$$

where $\mu_0 = 0.14$ GeV and $C_0 = -13.26$. Note that this parametrization of $D_{\gamma/Q'}(z,\mu_f)$ is an exact solution to the evolution equation at $\mathcal{O}(\alpha)$, so that the dependence on the fragmentation scale μ_f cancels exactly in our calculation. In the GGP analysis [24], other parametrizations of $D_{\gamma/Q'}(z,\mu_f)$ with different assumptions were compared, with only a small effect on the calculated cross sections.

One of the disadvantages of having a dependence on the quark-to-photon fragmentation function, in addition to the uncertainties due to the phenomenological fit to the function, is that it assumes that the cross section is inclusive in the fragmentation remnant. In our calculation, the combination of the experimental constraints on the photon and on the lepton indirectly imposes constraints on the remnant quark in the process. Therefore, we also consider an alternative model of the experimental isolation cut, replacing it with a "smooth" isolation cut [30], so as to avoid the necessity of the fragmentation contribution. The smooth isolation cut is given by requiring that the hadronic energy E_h inside all cones of radius $r < R$ around the photon direction satisfy

$$E_h < \epsilon E_\gamma \left(\frac{1-\cos r}{1-\cos R}\right), \tag{29}$$

where we take $R = 1$ and $\epsilon = 1/9$. These values of R and ϵ are chosen to ensure that the photon will contain at least 90% of the energy inside a cone of $r = 1.0$ centered on the photon, just as for the experimental isolation cut. However, the smooth cut does not translate exactly to the experimental isolation cut, because it requires the photon to carry a greater fraction of the energy as the cone size r becomes smaller. In practice, because of this, the theoretical calculation with the smooth cut is better behaved than with the sharp cut. In addition, the smooth isolation cut is more restrictive than the sharp isolation; for a strictly positive-definite differential cross section, the smooth isolation prescription must always give a smaller predicted cross section. In this way, a comparison of the two calculations can give some indication of the theoretical uncertainty due to the isolation cut.

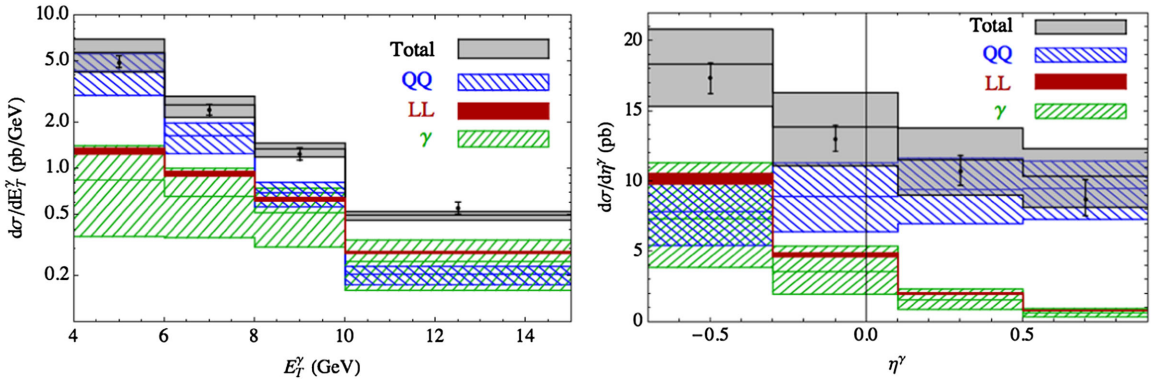

FIG. 4. Differential distributions for a zero initial inelastic photon PDF, using the smooth isolation prescription. The various bands display a variation in factorization scale between $0.5E_{\perp\gamma} \leq \mu_F \leq 2E_{\perp\gamma}$ and correspond to the total prediction (light gray solid), the QQ component (blue hashed), the LL component (dark red solid), and the photon-initiated contribution only (green hashed). Also shown are the ZEUS data points with combined statistical and systematic errors.

Finally, we note that the jet-clustering algorithm also includes the electron, so that the isolation cut effectively imposes $\Delta R_{\gamma e} > 1$.

D. Comparison with the data and constraints on the photon PDF

Before discussing the comparison of the theory with the data, it is useful to understand the theoretical uncertainties of the calculation by studying the factorization scale dependence and the dependence on the isolation prescription. In Fig. 4 we plot the differential cross sections for $d\sigma/dE_{\perp\gamma}$ and $d\sigma/d\eta_\gamma$ as functions of $E_{\perp\gamma}$ and η_γ, respectively, while varying the factorization scale within $0.5E_{\perp\gamma} \leq \mu_F \leq 2E_{\perp\gamma}$. Here we have used the sharp isolation cut and calculated with zero initial inelastic photon PDF at $Q_0 = 1.295$ GeV. The four bands on each of the two plots correspond to the photon-initiated contribution only (green hashed band), the LL component (dark red solid band), the QQ component (blue hashed band), and the total calculation (light gray solid band). The QL contribution is imperceptible on the scale of these plots. From these plots we learn several important facts. First, the scale dependence of the LL component is reduced dramatically compared to the photon-initiated contribution alone. This large scale dependence of the photon-initiated contribution cancels greatly with that of the collinear subtraction counterterm in the combined LL component. Second, the LL and QQ components dominate in different regions of phase space. For instance, the cross sections are most sensitive to the LL component, and consequently to the photon PDF, at large $E_{\perp\gamma}$ and small η_γ. Thus, the shapes of these distributions can give information about the nonperturbative contribution to the photon PDF. Finally, we note that the scale dependence of the QQ component is still large, being only LO in α_s, and it dominates the overall scale uncertainty of the theoretical calculation.

In Fig. 5 we plot the total predictions of the same two distributions, again for zero initial inelastic photon PDF, but now comparing the two different isolation prescriptions in the theoretical calculation. In these plots we show the predictions with the smooth isolation prescription (blue

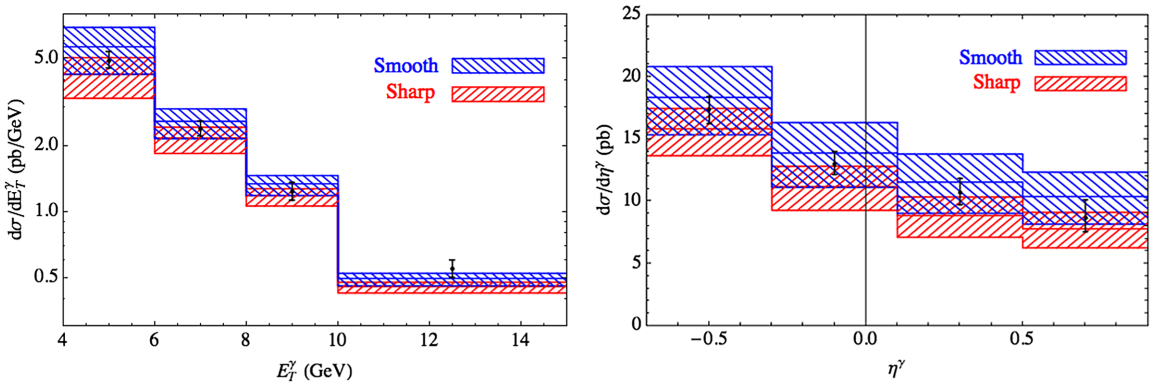

FIG. 5. Differential distributions for a zero initial inelastic photon PDF with the factorization scale varied between $0.5E_{\perp\gamma} \leq \mu_F \leq 2E_{\perp\gamma}$. The blue hashed band is calculated using the smooth isolation prescription, and the red hashed band is calculated using the sharp isolation prescription. Also shown are the ZEUS data points with combined statistical and systematic errors.

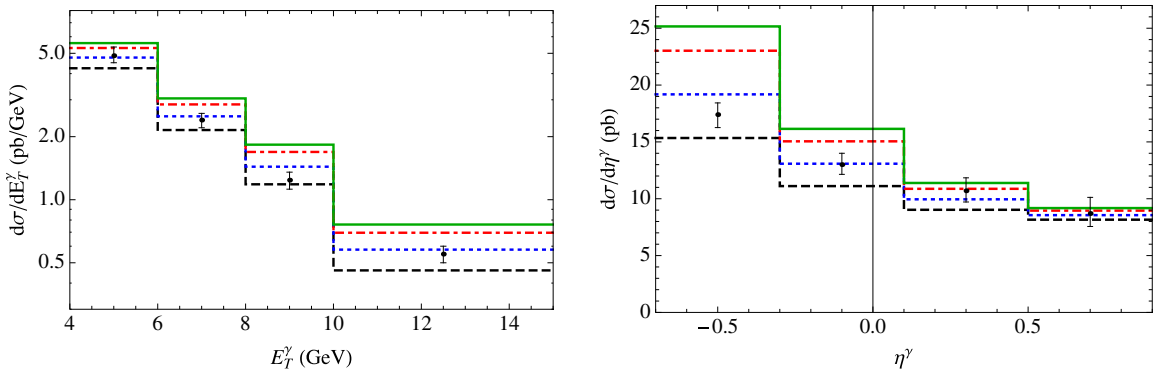

FIG. 6. Differential distributions in the photon variables, $E_{\perp\gamma}$ and η_γ, with the smooth isolation prescription, with factorization scale $\mu_F = 0.5E_{\perp\gamma}$. The curves, from bottom to top, are with initial inelastic photon momentum fractions of $p_0^\gamma = 0\%$ (black dashed), 0.1% (blue dotted), 0.2% (red dot-dashed), and for the CM photon (green solid). Also shown are the ZEUS data points with combined statistical and systematic errors.

hashed band) and the sharp isolation prescription (red hashed band), again varying the factorization scale within $0.5E_{\perp\gamma} \leq \mu_F \leq 2E_{\perp\gamma}$. The first thing to note here is that the difference between the predictions is about the same size as the scale uncertainty, with similar dependence on the kinematic variables. Another striking feature is that the prediction using the smooth isolation prescription is uniformly larger than that using the sharp isolation, in contrast to expectations. This is probably due to incomplete cancellations in the sharp isolation calculation between the large negative collinear fragmentation contribution and the positive real contribution, due to indirect constraints on the emitted final-state quark in the real emission contribution. Presumably higher-order QCD corrections will affect the predictions for both isolation predictions, to resolve this issue. As noted previously, our calculation is only LO in α_s; we expect both the factorization scale uncertainty and the isolation prescription discrepancy to be reduced at NLO in α_s. In any event, we will use the two isolation prescriptions, as well as the factorization scale dependence, as a measure of the theoretical uncertainty of our calculation.

With this understanding of the theoretical uncertainties of the calculation, we can now compare the ZEUS data against predictions for the differential distributions, while varying the initial inelastic photon momentum fraction p_0^γ of the photon PDF, described in Sec. II B. For this analysis, the initial quark and gluon PDFs are just the CT14NLO PDFs, except that the sea-quark normalizations are rescaled in order to maintain a total momentum fraction of 1. This rescaling has little effect in our analysis, because the photon momentum fractions considered here are small. For instance, a photon momentum fraction of $p_0^\gamma = 0.14\%$ induces a reduction of the sea-quark momentum by only 0.9%, while the CM photon PDF induces a reduction of the sea-quark momentum by 1.6%. At this stage of the analysis we have not refit the quark and gluon PDFs, since the $ep \to ep + X$ process is dominantly sensitive to the photon PDF directly, whereas the indirect sensitivity through changes in the quark and gluon PDFs is negligible.

In Fig. 6 we plot the differential cross sections for $d\sigma/dE_{\perp\gamma}$ and $d\sigma/d\eta_\gamma$ as a function of the photon variables, $E_{\perp\gamma}$ and η_γ, using the smooth isolation prescription, with a factorization scale of $\mu_F = 0.5E_{\perp\gamma}$. The curves, from bottom to top, are with initial inelastic photon momentum fractions of $p_0^\gamma = 0\%$ (black dashed), 0.1% (blue dotted), 0.2% (red dot-dashed), and for the CM initial photon (green solid), which has initial momentum fraction 0.26%. Also shown are the ZEUS data points with combined statistical and systematic errors. With these choices of μ_F and the isolation prescription, we see that the theory can fit the data well for $p_0^\gamma \approx 0.1\%$. On the other hand, the theory fits poorly for the CM initial photon, overshooting the data at large $E_{\perp\gamma}$ and small η_γ. Of course, the best fit for p_0^γ is correlated with the choice of μ_F and the isolation prescription. However, since these choices tend to move the curves up or down uniformly, it is still possible to constrain the initial photon PDF by the shape of the distributions. In particular, it is impossible to get a good fit to the prediction using the CM initial photon PDF, regardless of the choices of μ_F and the isolation prescription.

In Fig. 7 we plot the differential cross sections for $d\sigma/dQ^2$ and $d\sigma/dx$ as a function of the lepton variables, Q^2 and x, against the ZEUS data, using the exact same theoretical choices and initial inelastic photon PDFs as for the previous plot. In this case we see that it is impossible to fit the data, regardless of the initial photon PDF or the choices of factorization scale and isolation prescription. In particular, the theory fits the data very poorly at small x and Q^2. In fact, we note that prediction for the smallest bin in x is far from the ZEUS data point and is essentially independent of the initial photon PDF. We expect that the predictions in these bins are highly sensitive to higher-order QCD radiation, so that it is difficult to fit the full lepton distributions with a fixed-order calculation.

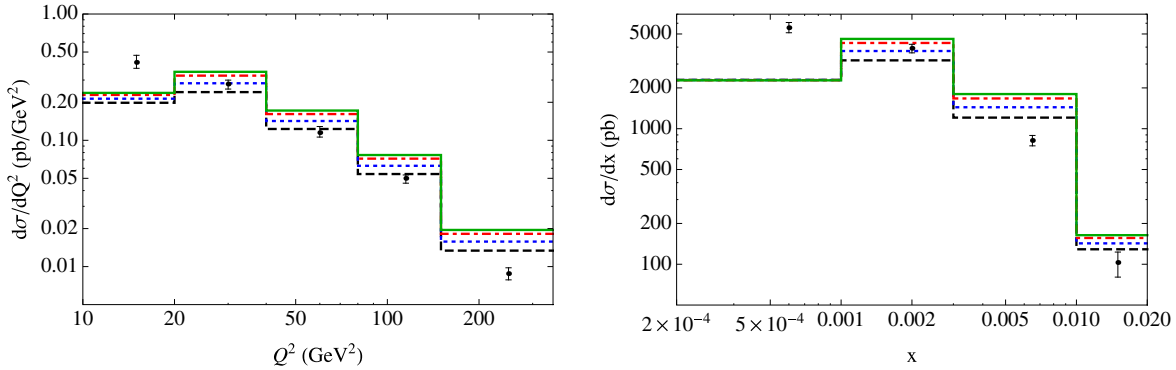

FIG. 7. Differential distributions in the lepton variables, Q^2 and x, with the smooth isolation prescription, with factorization scale $\mu_F = 0.5Q$. The curves, from bottom to top, are with initial inelastic photon momentum fractions of $p_0^\gamma = 0\%$ (black dashed), 0.1% (blue dotted), 0.2% (red dot-dashed), and for the CM photon (green solid). Also shown are the ZEUS data points with combined statistical and systematic errors.

The fact that these fixed-order calculations are more reliable for the photon distributions than for the lepton distributions can be seen further by looking at the phase-space constraints for the two sets of variables. In Fig. 8 we show plots of the constraints on the photon variables $E_{\perp\gamma}$ and η_γ and on the lepton variables Q^2 and x. In these figures, the dashed lines indicate the bins that are plotted by the ZEUS data. The combined dark red and light blue regions indicate the regions of phase space allowed by the ZEUS kinematic constraints of Eq. (27), for the fully inclusive event, whereas the dark red region only is allowed for the LO photon-initiated subprocess. For the photon distributions, the constraints are dominated by the photon cuts on $E_{\perp\gamma}$ and η_γ, with only a small cut on the photon-initiated contribution in the upper-left corner due to the requirement of $\eta'_\ell < -1.0053$. Thus, all of the bins in $E_{\perp\gamma}$ and η_γ have a large photon-initiated contribution and can be considered very inclusive. In contrast, for the lepton distributions, the additional photon constraints have a large effect in many of the bins. For instance, the photon-initiated contribution to the smallest Q^2 bin is largely removed by the requirement of $E_{\perp\gamma} > 4$ GeV, and the photon-initiated contribution to the smallest x bin is completely removed by the requirement of $\eta_\gamma > -0.7$. These bins are dominated by events with additional particles in order to satisfy the kinematics, so we would not expect our fixed-order calculation to do well at predicting the lepton distributions.

Based on these arguments, we will use only the distributions in the photon variables $E_{\perp\gamma}$ and η_γ to constrain the initial inelastic photon PDF, for a total of eight data points. We also reiterate that the constraints due to the

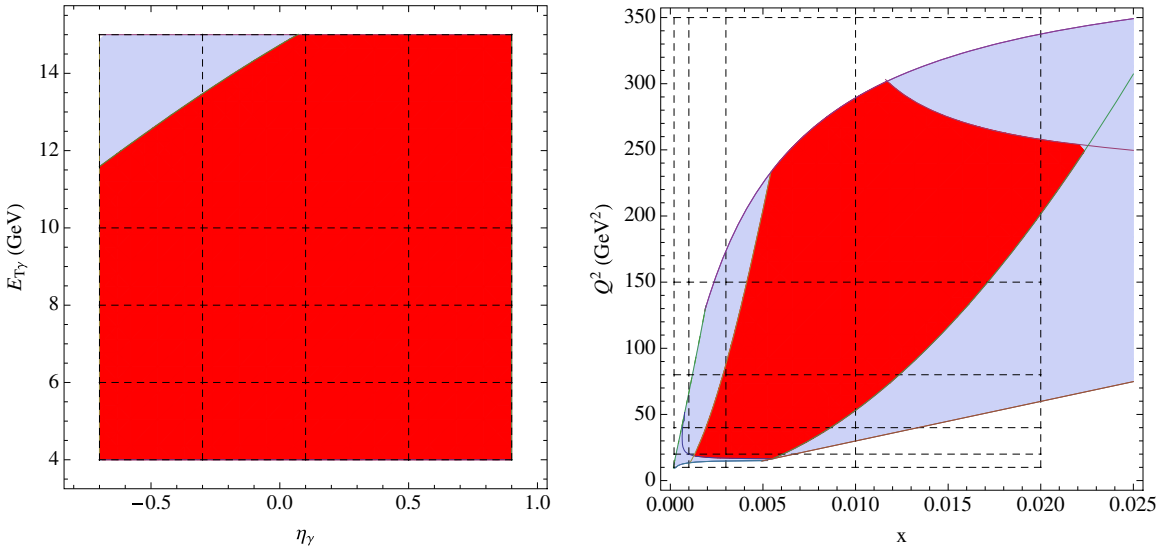

FIG. 8. Kinematic limits on $E_{\perp\gamma}$ and η_γ (left) and Q^2 and x (right). The dashed lines indicate the bins that are plotted by the ZEUS experiment. The dark red region only is kinematically accessible by the photon-initiated contribution, while the dark red and light blue regions are kinematically allowed in general.

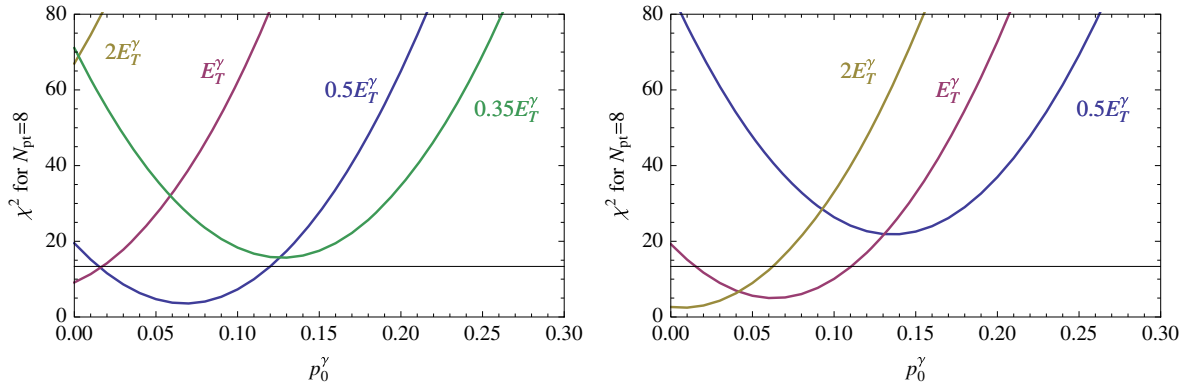

FIG. 9. Plots of χ^2 versus initial inelastic photon momentum fraction p_0^γ using the smooth isolation prescription (left) and the sharp isolation prescription (right) for factorization scales $\mu_F = 2E_{\perp\gamma}$, $E_{\perp\gamma}$, $0.5E_{\perp\gamma}$, and $0.35E_{\perp\gamma}$. The horizontal line at $\chi^2 = 13.36$ is the 90% confidence level limit for eight data points.

remaining CT14 experimental data set are much weaker than these data, and are neglected in the present analysis. We define the chi-squared function for these data points by

$$\chi^2 = \sum_{i=1}^{8} \left(\frac{T_i - D_i}{\sigma_i} \right)^2, \tag{30}$$

where T_i, D_i, and σ_i are the theory prediction, the experimental measurement, and its combined statistical and systematic error for the data point i. In Fig. 9 we plot χ^2 versus the initial inelastic photon momentum fraction p_0^γ for both the smooth and sharp isolation prescriptions and for several values of the factorization scale μ_F. Note that the value of p_0^γ determined by the minimum of χ^2 depends significantly on the isolation prescription and on the factorization scale, giving best fits for the initial momentum fraction that can vary from less than 0 to above 0.1%. In addition, due to this theoretical uncertainty in the current calculation, it is not possible to unambiguously determine an error band on p_0^γ using the standard CT approach of applying some tolerance criterion on the rise in the χ^2 around the best fit. However, from Fig. 9 we do see that not all choices of theoretical parameters are able to fit the shape of the data points equally well. Therefore, we can determine a conservative limit on the value of p_0^γ by requiring that the data and theory not disagree beyond some level. A χ^2 distribution with eight data points will have $\chi^2 < 13.36$ at the 90% confidence level.[5] Therefore, we define that any theoretical prediction with $\chi^2 > 13.36$ is ruled out as a bad fit to the data at the 90% confidence level. It is impossible to satisfy this criterion for $p_0^\gamma > 0.14\%$ for either choice of the isolation prescription and for any value of μ_F. Furthermore, we find that the CM choice of the photon PDF has $\chi^2 > 46$ for any choice of isolation and factorization scale and so is ruled out by this data.

Thus, we find our maximal initial inelastic photon PDF to have $p_0^\gamma = 0.14\%$ at the 90% confidence level. Of course, the exact value of the momentum fraction is correlated with the shape of the initial photon PDF. From Fig. 8 we see that the ZEUS DIS-plus-isolated-photon data constrains the photon PDF in the kinematic region given roughly by $10^{-3} < x < 2 \times 10^{-2}$ for $16 < Q^2 < 300$ GeV^2. Outside of this region, the photon PDF is very weakly constrained, but we believe that the radiative ansatz gives a reasonable expectation for its overall shape. As for the minimal possible value of the initial inelastic photon momentum fraction, it could, in principle, be negative, which is not ruled out by the analysis of this section. For instance, one could begin the evolution with zero initial photon PDF at a lower value of the scale

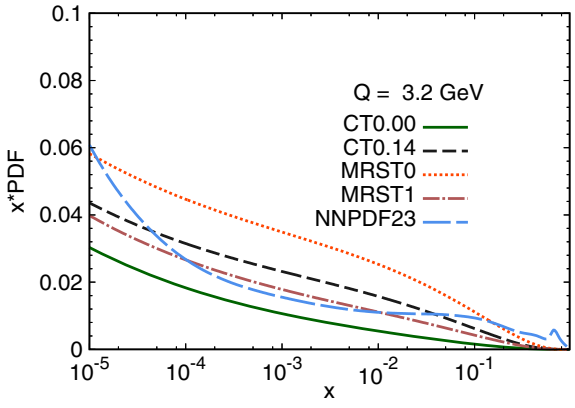

FIG. 10. Comparison of various NLO photon PDFs at the scale $Q = 3.2$ GeV: CT14QED with $p_0^\gamma = 0\%$ (solid green), CT14QED with $p_0^\gamma = 0.14\%$ (short-dashed black), MRST2004QED0 using current quark masses (dotted orange), MRST2004QED1 using constituent quark masses (dot-dashed brown), and NNPDF2.3QED with $\alpha_s = 0.118$ and average photon (long-dashed blue).

[5]As a comparison, the change in the total χ^2 for the remaining 2947 data points used in the CT14 analysis is $\Delta\chi^2 = -2.3$ in going from $p_0^\gamma = 0\%$ to $p_0^\gamma = 0.14\%$.

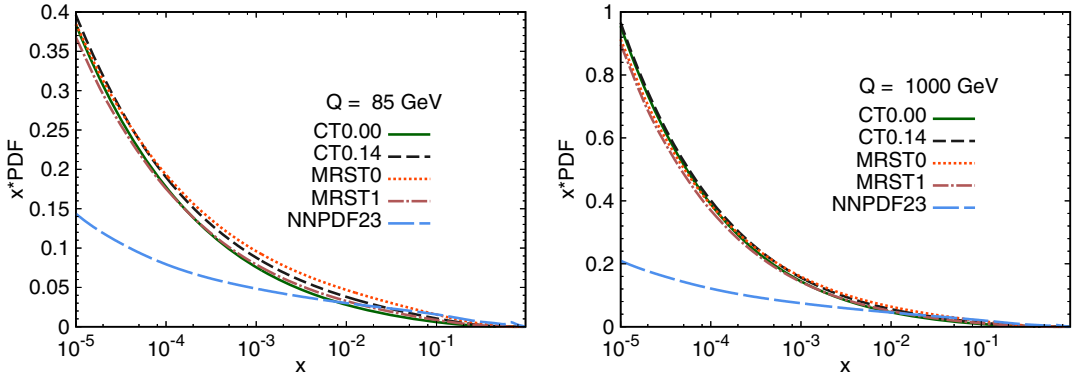

FIG. 11. Comparison of various NLO photon PDFs at the scales $Q = 85$ GeV (left) and $Q = 1$ TeV (right): CT14QED with $p_0^\gamma = 0\%$ (solid green), CT14QED with $p_0^\gamma = 0.14\%$ (short-dashed black), MRST2004QED0 using current quark masses (dotted orange), MRST2004QED1 using constituent quark masses (dot-dashed brown), and NNPDF2.3QED with $\alpha_s = 0.118$ and average photon (long-dashed blue).

Q_0. However, we take the reasonable assumption that it should be nonzero at the low scale of $Q_0 = 1.295$ GeV. We thus propose the initial PDFs with $p_0^\gamma = 0\%$ and $p_0^\gamma = 0.14\%$ as our 90% C.L. photon PDFs. A similar analysis gives $p_0^\gamma \leq 0.11\%$ at the 68% confidence level, but the data are still consistent with $p_0^\gamma = 0\%$ at the 68% C.L.

In Fig. 10 we compare, at the scale $Q = 3.2$ GeV, the CT14QED photon PDFs with $p_0^\gamma = 0\%$ and $p_0^\gamma = 0.14\%$ against the NLO MRST2004QED photon PDFs, using the current quark masses (labeled MRST0) and using the constituent quark masses (labeled MRST1), and against the NLO NNPDF2.3QED average photon PDF with $\alpha_s = 0.118$. We should emphasize that the CT14QED photon PDFs only contain the inelastic contribution in these plots. The NNPDF2.3 average photon PDF has more structure in its shape at large and small values of x than do the other PDFs, but it is still consistent with the ZEUS data in the x range that is probed by the experiment.

In Fig. 11 we compare the same set of photon PDFs at the higher scale of 85 GeV and the very high scale of 1 TeV. Here we can make some very interesting observations. The most obvious thing in these figures is that the CT and MRST photon PDFs become very similar at large Q^2, whereas the NNPDF photon PDF is distinctly different and much smaller at small values of x. This difference is due to the different approaches to the evolution of the PDFs taken by the different groups. Whereas in the MRST and CTEQ-TEA approaches, the QCD and QED scales are chosen to be identical and evolved together, in the NNPDF2.3QED PDFs that are included in the LHAPDF library [31], the QCD and QED scales are separate and the two scales are evolved successively; first the QED scale is evolved from Q_0 to Q, and then the QCD scale is evolved from Q_0 to Q. As discussed in Ref. [8], the successive evolution of QED and QCD differs from the combined evolution by terms that are subleading by $\mathcal{O}(\alpha\alpha_s)$ and can induce large unresummed logarithms between the two scales. This difference in the evolution at small x is also seen to be consistent with the behavior seen in the right panel of Fig. 2 in Ref. [6], where the NNPDF photon PDF also is smaller at small x and large Q^2 than when it is evolved using the code partonevolution [7,18]. We expect that the difference between the NNPDF2.3QED photon PDF and the other photon PDFs at high Q would be less significant if the NNPDF2.3QED PDFs were evolved from the low scale simultaneously in QED and QCD.

Another observation from Fig. 11, concerning the CT14QED and MRST2004QED photon PDFs, is that the impact of the initial photon distribution becomes less significant as Q^2 increases and more photons are produced through radiation off the quarks. From these plots we see that the fractional deviation between the different photon PDFs decreases with increasing Q^2. In fact, at very small x and large Q^2, the differences in the sea-quark distributions of the PDFs presumably have more impact on the photon PDF than does the initial photon distribution.

IV. DISCUSSION AND CONCLUSION

In this paper, we have presented CT14QED, which is the first set of CT14 parton distribution functions obtained by including QED evolution at leading order (LO) with next-to-leading-order (NLO) QCD evolution in the global analysis by the CTEQ-TEA group. This development will provide better theory predictions to compare with the precision data, such as Drell-Yan pair production, measured at the LHC. The CT14QED PDFs are based on the CT14 NLO initial distributions with the addition of an initial photon PDF. (There is also an inconsequential rescaling of the quark-sea PDFs, in order to maintain the momentum sum rule.) The inelastic contribution to the photon PDF is parametrized at the initial scale Q_0 using a generalization of the radiative ansatz introduced by the MRST group in their previous study. The initial photon PDF then depends on two independent parameters [cf. Eq. (1)], which are related to the scales at which the radiation off the up and down valence quarks is cut off. However, given the weak

constraints on the initial photon PDF, we find it convenient at this time to set the scales equal, so that the initial photon PDF is parametrized by a single parameter, which we take to be the momentum fraction carried by the inelastic photon at the initial scale Q_0. For comparison purposes, we have also defined a "current mass" (CM) photon PDF, comparable to the MRST current mass PDF, for which the initial photon momentum fraction is $p_\gamma^0 = 0.26\%$.

A set of neutron PDFs can also be obtained with a small amount of isospin breaking, suggested by the radiative ansatz applied to first order in α, and which automatically ensures that the number and momentum sum rules are satisfied. However, as previously seen by both the MRST and NNPDF groups, we find that the constraints from isospin violation effects (generally small and most important at large x) in nuclear scattering and from the requirement of the momentum sum rule, imposed by the DIS and Tevatron data in the CT14, are relatively weak.

Thus, in order to constrain the photon PDF, we focused on the scattering process $ep \to e\gamma X$, which was measured by the ZEUS experiment at HERA. This process is dominantly sensitive to the inelastic photon PDF directly, with negligible indirect sensitivity through the modification of the quark and gluon PDFs by QED effects. It also has the advantage that the initial-state photon subprocess contribution occurs at leading order, so that it does not compete with other much larger contributions. In this paper we have produced for the first time a consistent and systematic calculation for this cross section that combines both the photon- and quark-initiated subprocesses, and simultaneously reduces the factorization scale dependence of either calculation. Details of this calculation were presented in Sec. III B. The photon isolation cut, which required that the final-state photon must contain at least 90% of the energy in the jet to which it belongs (where jets are formed with the k_T cluster algorithm with parameter $R = 1.0$), was modeled using two different models of photon isolation. We used the two different isolation prescriptions, as well as the factorization scale dependence as a measure of the theoretical uncertainty of our calculation.

By comparing the ZEUS data for the distributions of transverse energy and pseudorapidity of the final-state photon against our calculation of the differential distributions, we were able to constrain the initial inelastic photon momentum fraction inside the proton to be $p_\gamma^0 < 0.14\%$ at the 90% confidence level. Hence, the CM choice of photon PDF has been ruled out by this data. For completeness, we also compared the CT14QED PDFs to some of the NLO (in α_s) photon PDFs published by the MRST and the NNPDF groups. Phenomenological applications of the CT14QED PDFs will be discussed in future publications.

As shown in Fig. 5, the theoretical uncertainties due to the factorization scale dependence and the isolation prescription are currently larger than the experimental uncertainties of the Zeus data. Thus, extending our calculation to NLO in α_s should be able to further constrain the initial photon PDF. This is a project that we are currently undertaking.

Parametrizations for the (inelastic photon) CT14QED PDF sets (both proton and neutron versions) will be distributed in a standalone form via the CTEQ-TEA Web site [32], or as a part of the LHAPDF6 library [31]. For backward compatibility with version 5.9.X of LHAPDF, our Web site also provides CT14 grids in the LHAPDF5 format, as well as an update for the CTEQ-TEA module of the LHAPDF5 library, which must be included during compilation to support calls of all eigenvector sets included with CT14 [33]. We will also distribute sets with the inclusive photon PDFs, CT14QEDinc. For the proton, CT14QEDinc at the initial scale Q_0 is the sum of the (inelastic) CT14QED and the elastic component of the photon PDF, given by the equivalent photon approximation. The proton CT14QEDinc PDFs are then evolved from Q_0 to Q as discussed in Sec. II A. For the neutron, CT14QEDinc is equal to CT14QED, since the neutron has zero electric charge, and therefore it has no elastic component of the photon PDF.

ACKNOWLEDGMENTS

This work was supported by the National Science Foundation under Grant No. PHY-1417326. We also thank Sayipjamal Dulat, Tie-Jiun Hou, Joey Huston, Pavel Nadolsky and Jianwei Qiu for helpful discussions.

APPENDIX: COMPARISON OF OUR QCD-PLUS-QED EVOLUTION CODE WITH OTHER CODES

We have checked our code against the public evolution code partonevolution [7,18], which also solves the evolution equations at LO in QED and NLO in QCD. The main difference (other than technicalities of implementation) in the partonevolution code is that it also includes the charged leptons as partons in the proton. Using the toy model of Ref. [34] with zero initial photon PDF, ensuring that all input parameters agree, using the same formulation for the running of α_s and α, and removing the lepton PDFs and their contribution to $\tilde{P}_{\gamma\gamma}^{(0)}$ from partonevolution, we find excellent agreement between the two programs. Evolving from $Q_0 = 1.3\,\text{GeV}$ to $\mu_F = 100$ GeV, we find differences of less than 0.2% over most of the range of x for all of the PDFs, including the photon. Reinstating the lepton PDF contribution to the evolution equations in partonevolution, which in principle should be included for consistency, we find their effects on the quark and gluon PDFs to be negligible, with changes of less than $10^{-3}\%$. The only noticeable effect is the reduction of the photon PDF by about 1% with mild x dependence, due to splitting of the photons into lepton-antilepton pairs. This is presumably much less than other uncertainties in our analysis, so it is reasonable to leave out the lepton PDF contribution in our code. The percent difference in our prediction for the photon PDF, relative

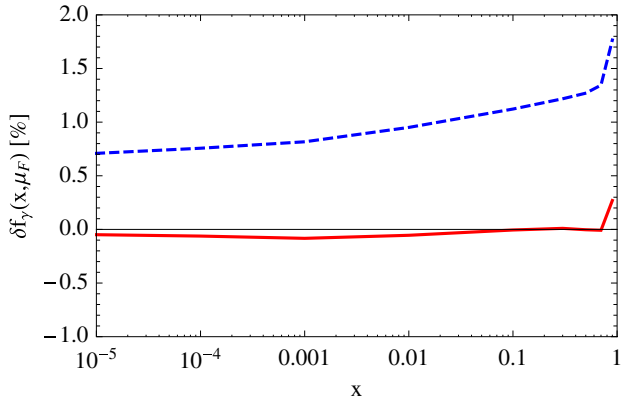

FIG. 12. Percent difference in our prediction for the photon PDF, relative to the partonevolution prediction, for the toy model parametrizations evolved from $Q_0 = 1.3$ GeV to $\mu_F = 100$ GeV, as discussed in the text. The solid red curve uses the partonevolution calculation with lepton PDFs removed from the evolution, while the dashed blue curve includes the lepton PDFs in partonevolution.

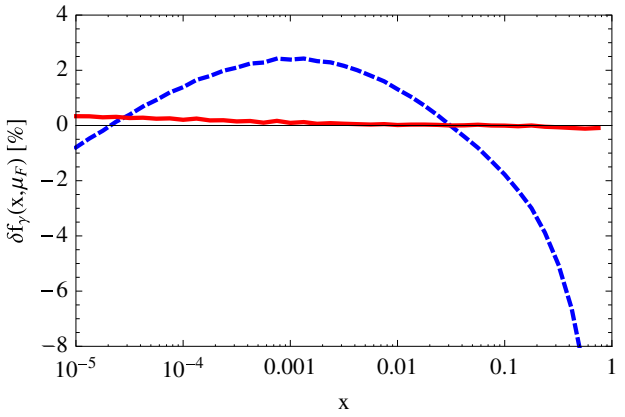

FIG. 13. Percent difference in our prediction for the photon PDF, relative to the prediction by APFEL with the "QUniD" setting (red solid) and "QavDP" setting (blue dashed). The PDFs are CT10NLO with zero initial photon PDF, evolved from $Q_0 = 1.3$ GeV to $\mu_F = 100$ GeV.

to the partonevolution prediction with and without the inclusion of the lepton PDFs, is shown in Fig. 12.

We have also checked our code against the program APFEL [8], which includes QED at LO and QCD at up to NNLO. The main difference in the APFEL program is that the QCD and QED factorization scales can be taken to be independent, and the evolution with respect to each scale can be done successively. However, using the setting "QavDP" in APFEL averages the two possible orderings for performing the evolutions, which should agree with our approach to $\mathcal{O}(\alpha^2)$. In addition, the APFEL code has been recently updated to allow the simultaneous evolution of the QED and QCD scales, using the "QUniD" setting. We have compared our code with APFEL 2.6.0, starting with the CT10NLO PDFs [20] with zero initial photon PDF at $Q_0 = 1.3$ GeV and evolving in QED at LO and QCD at NLO to $\mu_F = 100$ GeV. We have done the comparison using both the "QavDP" and the "QUniD" settings for APFEL. We obtain excellent agreement for the quark and gluon PDFs, with differences of less than 0.2% over most of the range of x for both APFEL settings. In Fig. 13 we show the results for the photon PDF. We obtain pretty good agreement with APFEL with the "QavDP" setting, with differences of less than 2.5% except at large $x > 0.1$. This is consistent with the $\mathcal{O}(\alpha^2)$ differences expected in the different evolution procedures. We obtain excellent agreement with APFEL with the "QUniD" setting, with differences of less than 0.34% over the full range of $x > 10^{-5}$ shown. We note that in Fig. 13 we replace the evolution subroutine for α in the APFEL program with the code used in the CT global analysis code; however, using the original α subroutine in APFEL still gives differences of less than 1% for the evolved photon PDF over the full range of x when using the "QUniD" setting. This is certainly much smaller than the uncertainties in the initial photon PDF itself.

We have not checked our code directly against the MRST evolution code or the recently developed `QCDNUM + QED` evolution code [35], but we do note that the comparison between `QCDNUM + QED` and APFEL "QavDP" for the evolution of the photon PDF in Ref. [35] looks qualitatively similar to the results that we have found in Fig. 13. In addition, benchmarking studies between APFEL and these two evolution codes in Ref. [36] show agreement at a similar level to that which we have found with our code here.

[1] S. Dulat, T.-J. Hou, J. Gao, M. Guzzi, J. Huston, P. Nadolsky, J. Pumplin, C. Schmidt, D. Stump, and C.-P. Yuan, Phys. Rev. D **93**, 033006 (2016).
[2] R. D. Ball *et al.* (NNPDF Collaboration), J. High Energy Phys. 04 (2015) 040.
[3] L. A. Harland-Lang, A. D. Martin, P. Motylinski, and R. S. Thorne, Eur. Phys. J. C **75**, 204 (2015).
[4] S. Alekhin, J. Blumlein, and S. Moch, Phys. Rev. D **89**, 054028 (2014).
[5] A. D. Martin, R. G. Roberts, W. J. Stirling, and R. S. Thorne, Eur. Phys. J. C **39**, 155 (2005).
[6] R. D. Ball, V. Bertone, S. Carrazza, L. Del Debbio, S. Forte, A. Guffanti, N. P. Hartland, and J. Rojo (NNPDF Collaboration), Nucl. Phys. **B877**, 290 (2013).

[7] M. Roth and S. Weinzierl, Phys. Lett. B **590**, 190 (2004).
[8] V. Bertone, S. Carrazza, and J. Rojo, Comput. Phys. Commun. **185**, 1647 (2014).
[9] A. D. Martin and M. G. Ryskin, Eur. Phys. J. C **74**, 3040 (2014).
[10] S. Chekanov *et al.* (ZEUS Collaboration), Phys. Lett. B **687**, 16 (2010).
[11] S. Moch, J. A. M. Vermaseren, and A. Vogt, Nucl. Phys. **B688**, 101 (2004).
[12] A. Vogt, S. Moch, and J. A. M. Vermaseren, Nucl. Phys. **B691**, 129 (2004).
[13] J. Pumplin, D. R. Stump, J. Huston, H. L. Lai, P. M. Nadolsky, and W. K. Tung, J. High Energy Phys. 07 (2002) 012.
[14] D. Stump, J. Huston, J. Pumplin, W.-K. Tung, H. L. Lai, S. Kuhlmann, and J. F. Owens, J. High Energy Phys. 10 (2003) 046.
[15] W. K. Tung, H. L. Lai, A. Belyaev, J. Pumplin, D. Stump, and C.-P. Yuan, J. High Energy Phys. 02 (2007) 053.
[16] P. M. Nadolsky, H.-L. Lai, Q.-H. Cao, J. Huston, J. Pumplin, D. Stump, W.-K. Tung, and C.-P. Yuan, Phys. Rev. D **78**, 013004 (2008).
[17] J. Pumplin, J. Huston, H. L. Lai, P. M. Nadolsky, W.-K. Tung, and C.-P. Yuan, Phys. Rev. D **80**, 014019 (2009).
[18] S. Weinzierl, Comput. Phys. Commun. **148**, 314 (2002).
[19] V. M. Budnev, I. F. Ginzburg, G. V. Meledin, and V. G. Serbo, Phys. Rep. **15**, 181 (1975).
[20] J. Gao, M. Guzzi, J. Huston, H.-L. Lai, Z. Li, P. Nadolsky, J. Pumplin, D. Stump, and C.-P. Yuan, Phys. Rev. D **89**, 033009 (2014).
[21] J. Blumlein, Z. Phys. C **47**, 89 (1990).
[22] J. Blumlein, G. Levman, and H. Spiesberger, J. Phys. G **19**, 1695 (1993).
[23] A. Arbuzov, D. Y. Bardin, J. Blumlein, L. Kalinovskaya, and T. Riemann, Comput. Phys. Commun. **94**, 128 (1996).
[24] A. Gehrmann–De Ridder, T. Gehrmann, and E. Poulsen, Phys. Rev. Lett. **96**, 132002 (2006).
[25] A. Gehrmann–De Ridder, T. Gehrmann, and E. Poulsen, Eur. Phys. J. C **47**, 395 (2006).
[26] M. A. G. Aivazis, J. C. Collins, F. I. Olness, and W.-K. Tung, Phys. Rev. D **50**, 3102 (1994).
[27] S. Catani and M. H. Seymour, Nucl. Phys. **B485**, 291 (1997); **B510**, 503(E) (1998).
[28] M. Forrest, Ph.D. thesis, University of Glasgow, 2010.
[29] D. Buskulic *et al.* (ALEPH Collaboration), Z. Phys. C **69**, 365 (1996).
[30] S. Frixione, Phys. Lett. B **429**, 369 (1998).
[31] https://lhapdf.hepforge.org/.
[32] http://hep.pa.msu.edu/cteq/public/ct14.html.
[33] http://hep.pa. msu.edu/cteq/public/ct14/lhapdf/v5/.
[34] J. Blumlein, S. Riemersma, M. Botje, C. Pascaud, F. Zomer, W. L. van Neerven, and A. Vogt, in *Proceedings of the Future Physics at HERA, Hamburg, Germany, DESY, 1996* edited by G. Ingelman, A. De Roeck, and R. Klanner (1996), pp. 23–32.
[35] R. Sadykov, arXiv:1401.1133.
[36] S. Carrazza, arXiv:1509.00209.